Particles I

Access the latest eBook →

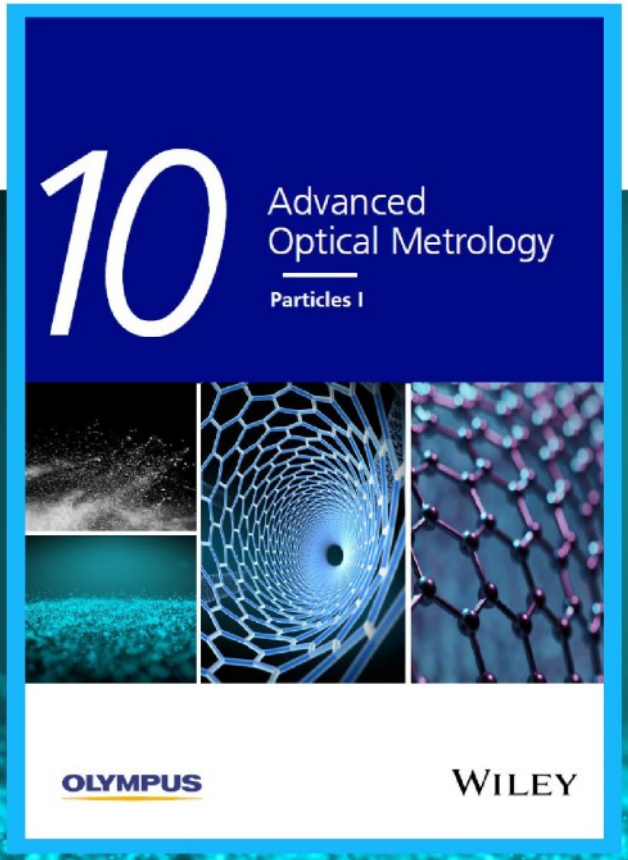

Particles: Unique Properties, Uncountable Applications

Read the latest eBook and better your knowledge with highlights from the recent studies on the design and characterization of micro- and nanoparticles for different application areas.

Access Now

This eBook is sponsored by

OLYMPUS

WILEY

ADVANCED MATERIALS
www.advmat.de

Searching for an Optimal Multi-Metallic Alloy Catalyst by Active Learning Combined with Experiments

Minki Kim, Min Young Ha, Woo-Bin Jung, Jeesoo Yoon, Euichul Shin, Il-doo Kim, Won Bo Lee, YongJoo Kim,* and Hee-tae Jung**

Searching for an optimal component and composition of multi-metallic alloy catalysts, comprising two or more elements, is one of the key issues in catalysis research. Due to the exhaustive data requirement of conventional machine-learning (ML) models and the high cost of experimental trials, current approaches rely mainly on the combination of density functional theory and ML techniques. In this study, a significant step is taken toward overcoming limitations by the interplay of experiment and active learning to effectively search for an optimal component and composition of multi-metallic alloy catalysts. The active-learning model is iteratively updated using by examining electrocatalytic performance of fabricated solid-solution nanoparticles for the hydrogen evolution reaction (HER). An optimal metal precursor composition of $Pt_{0.65}Ru_{0.30}Ni_{0.05}$ exhibits an HER overpotential of 54.2 mV, which is superior to that of the pure Pt catalyst. This result indicates the successful construction of the model by only utilizing the precursor mixture composition as input data, thereby improving the overpotential by searching for an optimal catalyst. This method appears to be widely applicable since it is able to determine an optimal component and composition of electrocatalyst without obvious restriction to the types of catalysts to which it can be applied.

1. Introduction

Fabrication of multi-metallic alloy catalysts is one of the most promising methods to boost catalytic performance, leading to synergistic performance that considerably surpasses the expectation from using only a simple combination of constituent elements.[1–7] However, determining the optimum elemental components and composition is challenging because of the different physical behaviors and chemical activities of the metal elements in catalytic reactions. Furthermore, it is difficult to determine the metal combination that must be investigated as it is difficult to exactly determine which metal element will affect the catalytic performance within the alloy. Before the introduction of computational techniques, researchers have mainly investigated binary and ternary alloys, with the focus on searching for high-performance multi-metallic catalysts by experimental trial and error.[8–10] For example, noble and non-noble metals, for example, platinum (Pt),[11–13] ruthenium (Ru),[14,15] iridium (Ir),[16,17] palladium (Pd),[18,19] and nickel (Ni),[20] iron (Fe),[21] cobalt (Co),[22] molybdenum (Mo),[23] as well as their alloys, are typically used in the hydrogen evolution reaction (HER), rendering the dimensionality of the space of alloy composition candidates far beyond human intuition or brute-force search by trial and error. However, it was almost impossible to search for the optimal component and composition for high-performance catalysts as the determination of the catalyst performance is a time-consuming and expensive process due to the enormous number of candidate combinations and compositions.

M. Kim, J. Yoon, H.-t. Jung
Department of Chemical and Biomolecular Engineering (BK21 four)
Korea Advanced Institute of Science and Technology (KAIST)
291 Daehak-ro, Yuseong-gu, Daejeon 34141, Korea
E-mail: heetae@kaist.ac.kr

M. Kim, J. Yoon, H.-t. Jung
Korea Advanced Institute of Science and Technology (KAIST) Institute for Nanocentury
Yuseong-gu, Daejeon 34141, Korea

M. Y. Ha, W. B. Lee
School of Chemical and Biological Engineering
Institute of Chemical Processes
Seoul National University
Seoul 08826, Korea
E-mail: wblee@snu.ac.kr

W.-B. Jung
John A. Paulson School of Engineering and Applied Sciences
Harvard University
Cambridge, MA 02138, USA

E. Shin, I.-d. Kim
Department of Materials Science and Engineering
Korea Advanced Institute of Science and Technology (KAIST)
291 Daehak-ro, Yuseong-gu, Daejeon 34141, Korea

Y. Kim
School of Advanced Materials Engineering
Kookmin University
Seoul 02707, Korea
E-mail: cjyjee@kookmin.ac.kr

The ORCID identification number(s) for the author(s) of this article can be found under https://doi.org/10.1002/adma.202108900.

DOI: 10.1002/adma.202108900

To overcome the "curse of dimensionality" in searching for the optimal alloy component and composition, researchers have recently employed computational techniques to narrow down the design space of multi-metallic alloy catalysts. Currently, approaches to search for the optimal component and composition of multi-metallic alloy catalysts rely on adsorption energy prediction by density functional theory (DFT) combined with advanced machine-learning (ML) algorithms,[24–27] where large-scale open databases[28,29] enable data-driven analysis and predictions of catalytic performance at the active sites with one or two metal components. For example, ML models trained with DFT data were successfully applied to predict the catalytic activity of bimetallic nanoparticles for nitric oxide (NO) decomposition,[30] methanol oxidation,[31] and carbon dioxide (CO_2) reduction.[32]

However, DFT-based ML calculations for multi-metallic active sites with three or more elements are limited by several major challenges. First, periodic unit cells in conventional DFT calculations assume a structure that is significantly different from the solid-solution structure of most alloys, which exhibit non-periodic atomic distributions.[33] Second, the final composition of the experimentally synthesized alloy is often different from the stoichiometric composition of the precursors,[34] and the ML model often lacks control over experimental process parameters, making it more difficult to correlate the computational predictions to experimental protocols. Third, the direct incorporation of nonmetallic components (e.g., carbon) into the metal active sites introduces serious complexity in terms of reliable calculations, although studies have reported that encapsulating graphene layers contribute to the catalytic performance.[35,36] Finally, computational calculations of multi-metallic unit cells are expensive owing to the necessity of large unit cells and the extensive requirement for k-vectors in the reciprocal space. As a result, errors from these uncertainties propagate through the computational process and introduce significant bias and epistemic uncertainty in the modeling; hence, the current metallic catalyst databases and ML techniques are not suitable for the universal exploration of multi-metallic alloy catalysts.

An alternative approach for DFT-based supervised ML calculations is introducing an active machine-learning model to directly predict the catalytic performances from experimentally adjustable parameters. Active learning is a machine-learning framework where a model closely cooperates with an "oracle," or the human user, by requesting points to be experimentally evaluated. The model suggestion is given on points with the maximum uncertainty so that each experimental evaluation leads to a large gain of information about the data space structure. Unlike in the conventional supervised machine-learning approach, where a large amount of training data should be gathered before the learning stage, active learning can reduce the required size of the training data up to several orders. Furthermore, since the model directly predicts the experimental outcome from adjustable process parameters, the model does not suffer from the bias inevitable in the DFT calculations.

In this study, a method that can search for an optimal component and composition of multi-metallic alloy catalysts for HER by a combination of experiment and active learning was demonstrated, where the model directly predicted the catalytic overpotential from experimentally adjustable parameters, namely the mole fraction of metal precursors used for nanoparticle synthesis by the carbothermal shock (CTS) method. With the CTS method, it was possible to fabricate multi-metallic alloys with atomic scale mixing, and with reduced time and cost. By selecting noble metals (e.g., Pt, Ru, Pd) and non-noble metals (e.g., Ni, Cu, Co, Fe, Tin (Sn)) for use in HER, active-learning iteration loops were conducted to locate the optimal composition of precursors that can exhibit the best catalytic performance in a data-efficient manner. In addition, the detailed evolution of the model was revealed in the course of iterations, and the most effective multi-metallic alloy catalysts were proposed to be screened by a simple method with time savings; this approach can be potentially applied to a wide variety of catalytic systems, which is difficult by the currently used DFT-based ML techniques.

2. Results

2.1. Active-Learning Model Construction

Figure 1 shows the overall scheme to search for the component and composition of a metal precursor that yields a sufficiently low overpotential for the HER by the combination of experiment and active learning. Here, an active-learning framework was utilized, involving the iterative cooperation of a model with a user to efficiently explore the design space of experimentally adjustable parameters.[37] The appropriate selection of a strategy and automatization of the experimental design by active learning can lead to a significantly faster and cost-effective strategy for the discovery of electrocatalysts with enhanced performance.[38,39] The input data for active learning (i.e., component and composition of metal precursor and measured overpotential) were obtained from the synthesis of multi-metallic alloy nanoparticles and their overpotential measurement by experiments. First, multi-metallic alloy catalysts were synthesized by the carbothermal shock (CTS) method[40] with varying mole fractions of metal in a precursor mixture (Figure 1a). Generally, it is known that some elements are thermodynamically immiscible and show phase separation using conventional synthesis techniques. Furthermore, fabricating one type of multi-metallic alloy nanoparticle usually takes a long time, up to several hours. However, the CTS method can fabricate multi-metallic nanoparticles without many limitations of element selection,[41] and can reduce time and cost for fabrication. It is reported that by the CTS method, it is possible to overcome the immiscibility of the bimetallic catalyst library. Thus, the CTS method allowed the random mixing of elements on the atomic scale and fabrication of a homogeneous nanoparticle size by rapid heating up to 2000 K[41] (Figure 1b). A detailed description of the CTS method is provided in Experimental Section. This method is suitable for searching for the optimal component and composition of multi-metallic alloy catalysts as the component and composition of the fabricated catalysts can be altered easily by the simple control of the metal precursor solution. After catalyst fabrication, electrochemical analysis was conducted to characterize the catalytic performance of the synthesized nanoparticles by measuring overpotential at a current density of 20 mA cm^{-2} via linear sweep voltammetry (Figure 1c). As locating the optimal precursor component and composition is a daunting task by this protocol, an active-

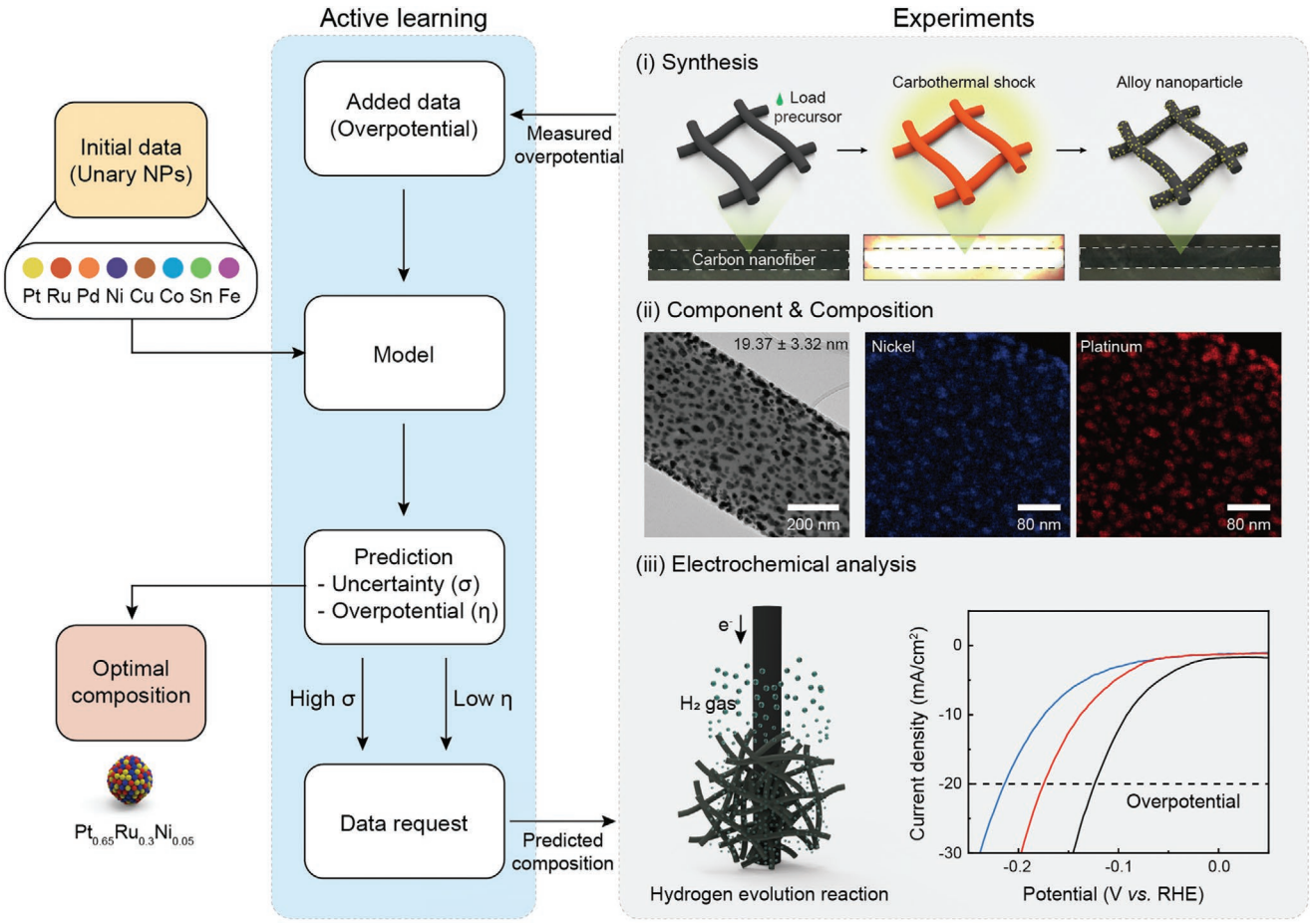

Figure 1. The overall workflow of searching for low-overpotential multi-metallic alloy catalysts. a) Brief schematic of the multi-metallic alloy nanoparticle synthesis and its corresponding photographical images. b) TEM image of well-synthesized alloy nanoparticles. c) Schematic image and linear sweep voltammetry curve for the electrochemical analysis of fabricated nanoparticles.

learning framework was employed by utilizing the mole fraction of the precursor component and overpotential data.

Active learning is an iterative process whereby an ML model interacts with an experimentalist to generate an optimal search trajectory in the design space; this approach is also called the optimal experiment design.[37] In this study, we train a Gaussian process (GP) model to learn a function that maps an 8D precursor composition vector to a scalar overpotential value; hence, the model directly predicts the experimental output from the experimental input, allowing the model to explicitly control the process parameters accessible to the user. Even though precursor composition and the mole fraction of the fabricated metal nanoparticles can be different, the machine considers the deviation between them as data are continuously accumulated. This is related to the ability of the machine that can inherently relate the input parameters with the other variables, affecting the model output. Thus, just by providing the precursor mixture composition as input to the machine, it can efficiently predict the overpotential of the system.

The GP model was chosen for two reasons. First, a GP model can readily evaluate the uncertainty of its prediction, given in terms of the diagonal elements of the covariance matrix, which is an essential component in the active-learning framework. Second, a GP model with a squared-exponential kernel is a universal approximator for any continuous function in the data space, given a sufficient amount of training data. Although extensive comparison and fine-tuning might yield a model that is potentially superior, by selecting a GP model, we minimize the underlying assumptions on the data space so that the methodologies developed in this work to be readily extended to future studies with different catalytic reactions or even multiple optimization objectives.

Briefly, the model is first trained with a small amount of data before the iteration loops begin: the first model is trained with 73 preliminary experimental data, which accounts for less than 0.6% of the discretized data space with a total of 12 404 points. (Figure 1). At each loop, the model yields two types of outputs at every candidate precursor composition: 1) prediction of the overpotential and 2) estimated uncertainty of the prediction. In the early stage of training with a few loops, the model lacks training data, making its prediction highly unreliable. Hence, it is beneficial for the user to perform experiments at points where the model returns the highest uncertainty, the results of which are fed back into the model to update the predictive performance. This allows the model to focus on subspaces where it has marginal knowledge, and the model acquires significantly

more information than that in the conventional supervised learning setup given the same amount of training data. By contrast, in the later stage of the iterations where the model uncertainty is sufficiently lower, the search strategy should be diversified to exploration and exploitation wings, where the model suggests points with the lowest expected overpotential, along with points with the highest uncertainty, to locate the candidate compositions for the optimal catalytic performance.

In this study, the model was first trained with initial data and was extended to ternary compositions. After three iteration loops in the ternary data space, the model uncertainty substantially decreased, with the experimental overpotential less than that of a pure Pt catalyst, which is the final goal in this study (bottom left box in Figure 1). At this stage, the active-learning iterations were terminated, and a detailed electrochemical analysis was performed to verify the catalytic performance of the discovered compositions. Detailed information on active learning is described in Experimental Section. In addition, further computational details can be found in Supporting Information.

2.2. Active Learning of Binary Systems

The "model" and "iteration" are defined and enumerated as follows. A "model" is a GP instance trained with the provided data, enumerated from the zeroth model that is trained only using the unary initial data. An *i*th "iteration" is a set of experimental observations made at the points requested by the *i*th GP model. For example, the second iteration is performed at the request of the second model, and the second model is updated with the experimental results of the second iteration to yield the third model. This procedure is iteratively performed until the model gathers sufficient information to return low-uncertainty predictions in the binary data space, after which the trained model is to be transferred to the ternary data space.

Figure 2 shows the evolution of model predictions for three representative binary systems, namely Pd–Ru, Pd–Ni, and Ru–Ni, during two iteration loops. These systems were selected as they clearly described the correlation between information among different metal combinations; this is a key feature related to the performance of the active-learning framework developed herein. When trained with only the unary data (initial data), the model fails to make any meaningful predictions for the binary data, as represented by the plateau shown in the first column of Figure 2. The unary data were augmented with 65 additional binary data scattered near the 50:50 mixture points for each binary combination to obtain the first model, from which active-learning iterations were commenced.

Figure 2 manifests two key trends. First, the uncertainty at the points requested by the model was considerably reduced after an iteration loop, which was an expected result. Second,

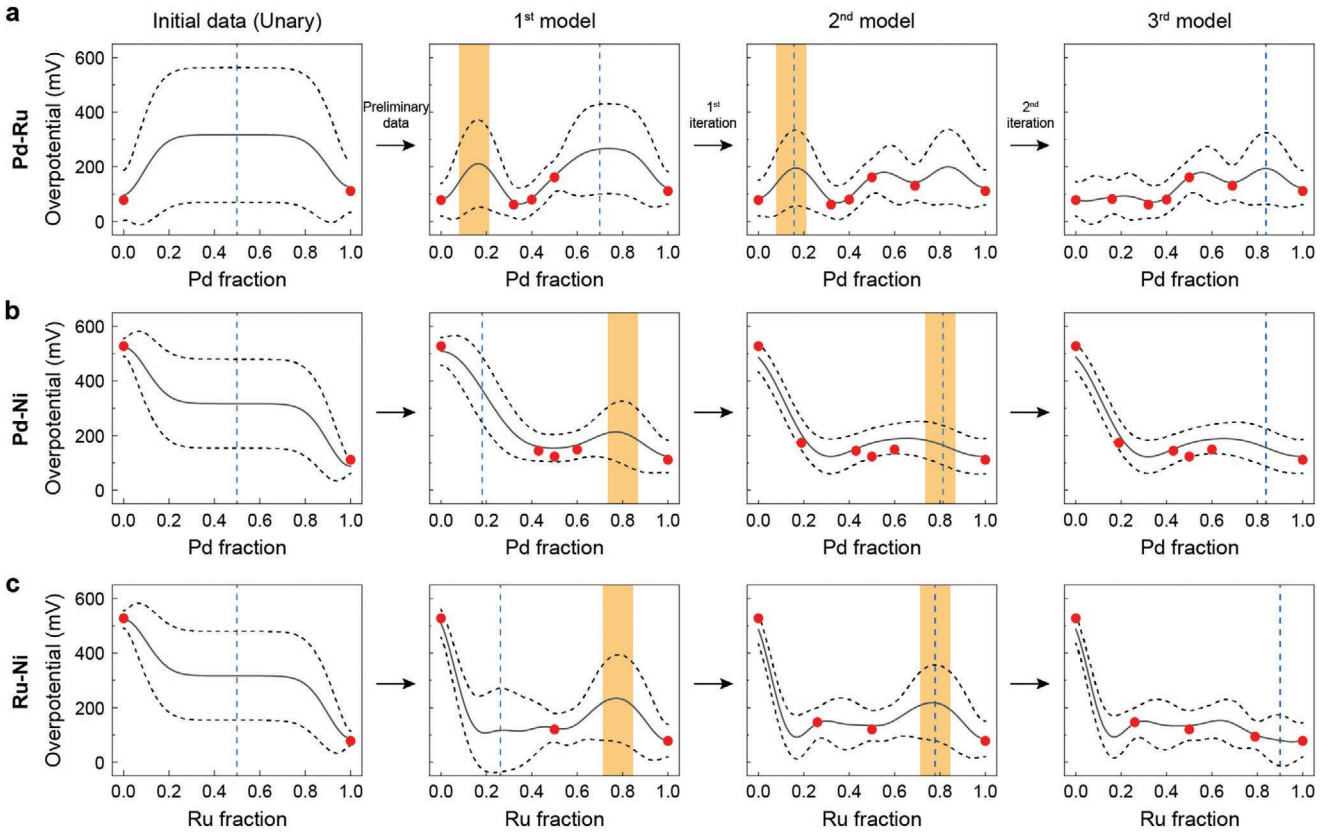

Figure 2. Active-learning results for binary composition. a–c) With each iteration, the prediction of the binary composition model of Pd–Ru (a), Pd–Ni (b), and Ru–Ni (c) changes. The orange areas highlight the change of prediction without the added data at certain points after the iteration. The vertical blue dashed lines indicate the points of maximum uncertainty in each binary composition: since 20 experimental results are fed into the model in each iteration, some points with maximum uncertainty may not be updated, as in the second iteration in (b).

notably, uncertainty was often reduced in regions that were not experimentally verified in the previous iteration (see orange regions in Figure 2). Owing to the Pd-rich phase data obtained in the first iteration of the Pd–Ru diagram (Figure 2a), the uncertainty of the Pd-rich phase decreased after the first iteration in Figure 2b. This indirect learning was possible as the model learned the universal data structure of the 8D composition vector space instead of learning individual curves for each binary combination (Supporting Information). Hence, the binary diagrams shown in Figure 2 are best understood as projections of the entire data space onto 1D binary subspaces, and the model effectively learns all of the mutual effects among different binary systems that are difficult to capture by human intuition. This interaction among different metal combinations is the key factor behind the performance of active learning.

After the second iteration, the model is confirmed to acquire sufficient information regarding the overpotential variation of the binary data space, and it is not likely to expect an overpotential significantly less than that of pure Pt nanoparticles. Hence, extending from the accumulated binary overpotential data, the third binary model is transferred to predict the HER overpotential of ternary composition spaces.

2.3. Active Learning of Ternary Systems

Figure 3 shows the evolution of model prediction for the Pt–Ru–Ni ternary system: this combination was selected because it contained the precursor composition with the lowest overpotential, that is, $Pt_{0.65}Ru_{0.30}Ni_{0.05}$. Unlike in the binary system,

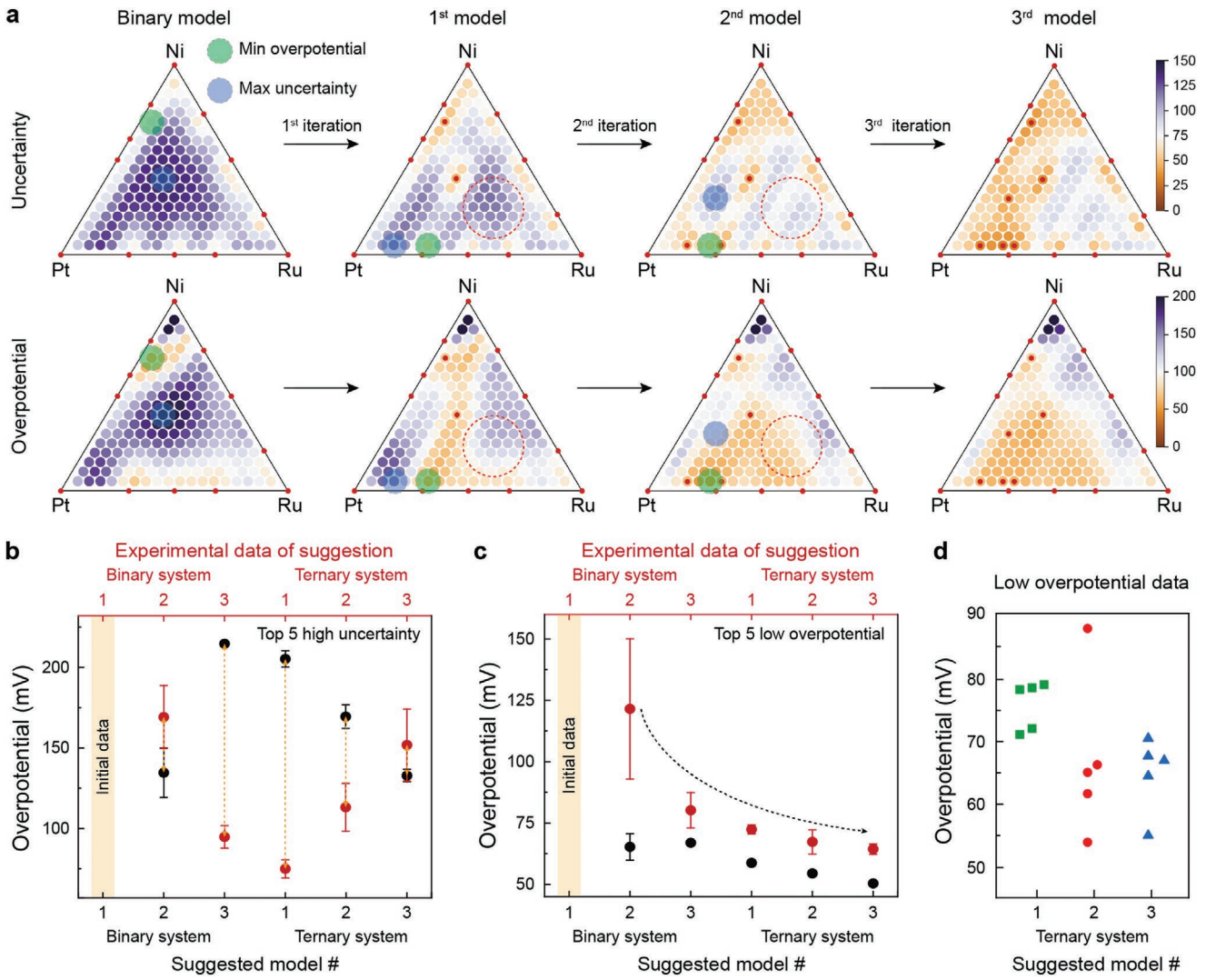

Figure 3. Active-learning results for a ternary composition. a) With each iteration, a triangular diagram of uncertainty and overpotential is updated for the Pt–Ru–Ni system. The red dotted circles indicate the change in prediction without data added at certain points after iteration. b) Plot of the overpotential of the top-five high-uncertainty points with active learning. The black and red circles indicate the experimental results and the prediction by the model, respectively. The orange arrows indicate the difference in the values between modeling and experimental data. c) Plot of overpotential of the top-five low-overpotential point changes with active learning and d) corresponding scatter-plotted ternary data points. Note that the data points in each ternary model belong to five different ternary combinations, and the distribution of these points is not necessarily continuous: hence, the distribution of the lowest overpotential within each model is subject to large variance, for example, as in the second ternary model.

where the search was only performed at the points with high uncertainty, an exploration–exploitation strategy was applied, where half of the experimental evaluations were made at points with the highest uncertainty, and the remaining half were performed at points with the lowest predicted overpotential (Figure 1). The two types of suggestion points are denoted by blue and green circles, respectively (Figure 3a).

The model trained only with the binary data revealed high uncertainties in the center of the triangular diagram (Figure 3a). After the first iteration, the uncertainty at the internal region of the triangular diagram was significantly decreased, especially near the experimentally verified points. After the model was updated in the second iteration, the uncertainty of the Pt–Ru–Ni system decreased in a wide range of the composition space. In particular, the uncertainty in the high-Ru area on the lower right of the diagram, which was enclosed by a red dotted circle, decreased significantly even without experimental observations due to the data added from other ternary combinations (e.g., Pd–Ru–Sn, Figure S11, Supporting Information). Moreover, the overpotential distribution after the second iteration revealed a nonlinear variation of overpotential within the ternary system, manifesting the "cocktail effect," which can be described as the synergistic effect resulting from mutual interactions among composing elements. This effect could bring excess quantities to the average values simply predicted by the mixture rule,[42] or sometimes the cocktail effect can work in a different way, which can also lead to nonlinear and unexpected properties due to unusual interstitial strengthening and intermetallic precipitation strengthening.[43] Overall, the mixture of elements can either work to result in excessive or unexpected properties, which was present in multi-metallic alloy systems. After the third iteration, the model did not exhibit considerable changes, indicating that the second and third models approach the saturation of training in the systems that are highly correlated to the Pt–Ru–Ni combination.

It should be noted that further iteration loops might be performed to locate ternary compositions with even better catalytic performances than the points located in the third model. In principle, the decision whether to continue or stop the active-learning iterations should be made by considering the balance between the expected improvement of future discoveries and the time and cost of experimental evaluations. In this work, we decided to break the iteration loop at the third model from two considerations. First, the saturation of the model performance as shown in Figures 3b,c implied that the expected improvement from further iterations would be smaller than in the early stage of the iteration loops. Second, as shown in Figure 3d, we already located several points superior to pure Pt, which is the benchmark for HER, indicating that a dramatic improvement of overpotential is unlikely in further iterations.

2.4. Overpotential Behavior with Iterations of Active Learning

The saturation behavior of the model was more clearly observed by comparing the predicted and experimentally measured overpotentials (Figures 3b,c). Figure 3b shows the change in the predictive performance of high-uncertainty suggestions. Notably, in high-uncertainty suggestion points, a large error between the predicted and experimental values is desired as the model would gain the maximum information at points it is gravely wrong. Before the iteration loops, prediction from the initial model was reasonably close to the experimental value. However, with the start of the iteration loops, the gap between the predicted and verified overpotentials considerably widened, especially in the third binary model and the first ternary model. With the increased accumulation of data, the prediction error slowly decreased, and at the end of the iteration loops, the third ternary model exhibited a considerably reduced prediction error even at the points with the highest uncertainty. In particular, compared to the difference between the model and experimental overpotential values of the first iteration in the ternary system (≈130 mV), the difference decreased to 56 mV at the end of the second iteration, with an even further decrease to 19 mV in the third iteration. This decrease in the difference between the model and actual experimental values reflected the increased accuracy of the model during the iteration.

This saturation behavior is also observed for predictions in the low-overpotential suggestion points shown in Figure 3c. In the second binary iteration, the experimental overpotential was extremely high even though the model expected them to be as low as 60 mV, indicating that the second binary model is considerably incorrect in estimating the points with high catalytic performances. After the third binary iteration, the verified overpotential was considerably reduced, and the predicted and verified overpotentials gradually decreased with the increase in the accumulated data. With the increase in the number of iteration loops, the model actually found an increasing number of points with a lower HER overpotential, indicating that the active-learning framework is leading the model in the right direction of locating the optimal composition for low overpotential. Figure 3d shows the scatter plot of the experimental data of low-overpotential points in ternary systems, again verifying the trend of the decreasing overpotential shown in Figure 3c. Figure S12, Supporting Information shows the scatter plots of the other measured overpotential data herein. The overall trend indicates that the overpotential tends to decrease with the increase in the system dimension from a unary to a ternary system. Thus, compared to unary and binary systems, ternary systems exhibit a significantly lower overpotential, reflecting the cocktail effect of multi-metallic alloy catalysts.

2.5. Characterization of Synthesized Catalysts

After all iterations, the optimal composition of the $Pt_{0.65}Ru_{0.30}Ni_{0.05}$ alloy catalyst with a remarkably low overpotential of 54.2 mV was found, and this catalyst was further investigated experimentally (**Figure 4**). First, the formation of Pt–Ru–Ni alloy nanoparticles was observed by transmission electron microscopy (TEM) (Figure 4a). These alloy nanoparticles were well dispersed over the substrate, with a uniform size of 9 ± 3.14 nm. The size of the nanoparticles was different from that of the Pt–Ni alloy (Figure 1), indicative of the change in the nanoparticle size owing to the different components and compositions of the metal precursor. In addition, Pt–Ru–Ni alloy formation was investigated by TEM–energy-dispersive

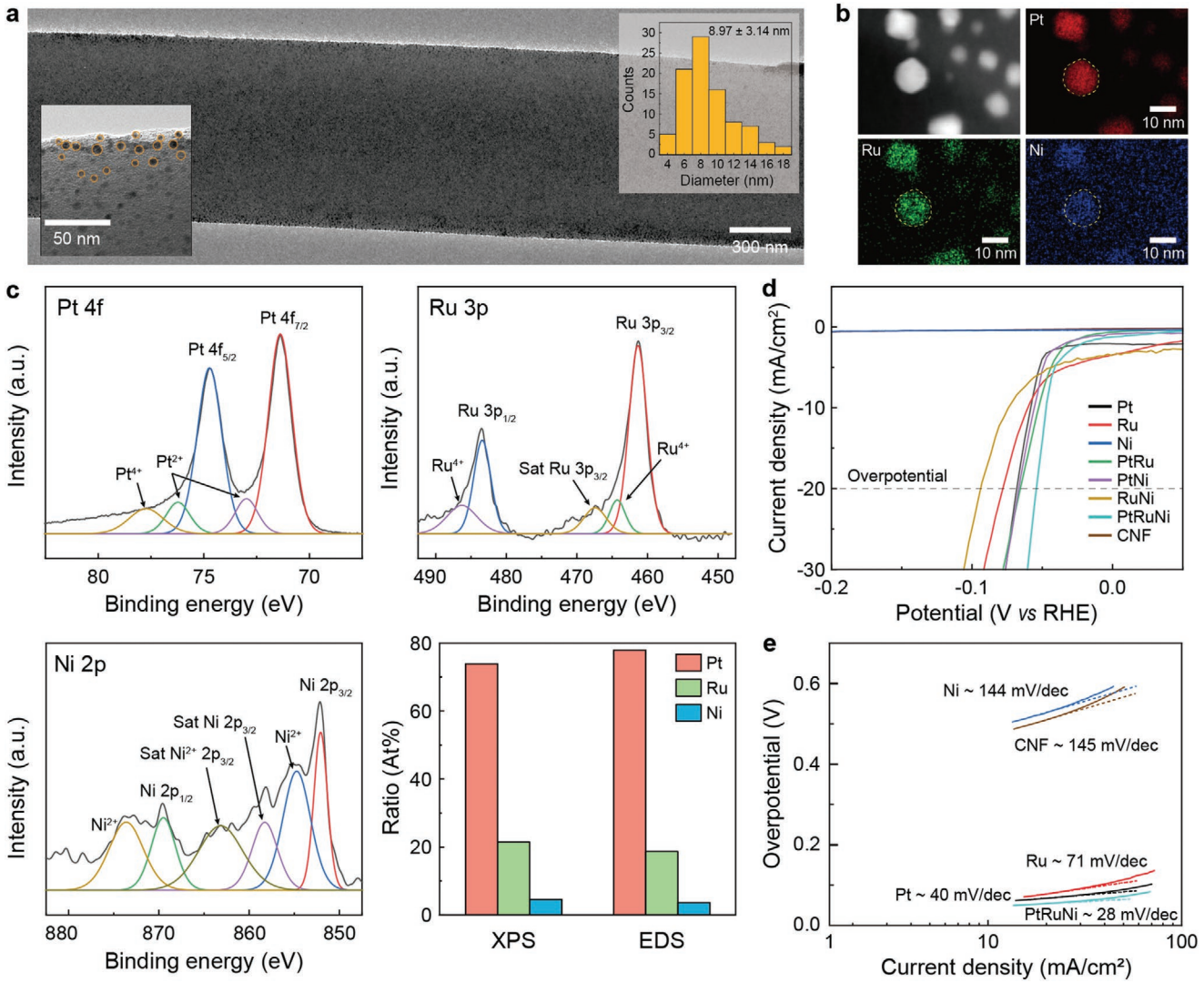

Figure 4. Characterization of Pt–Ru–Ni ternary nanoparticles by the carbothermal shock method. a) TEM image of well-synthesized Pt–Ru–Ni nanoparticles with an average size of 9 nm. b) TEM–EDS mapping of Pt–Ru–Ni nanoparticles. c) XPS spectra of Pt, Ru, and Ni after carbothermal shock and nanoparticle composition by different analysis methods. d) Polarization curves of different catalysts. The dotted line indicates the overpotential estimated herein. e) Tafel plot of different catalysts.

X-ray spectroscopy (TEM–EDS) mapping (Figure 4b): These fabricated metal nanoparticles comprised well-mixed Pt, Ru, and Ni, with an average nanoparticle diameter of ≈9 nm, suggesting that the three metals in the ternary nanoparticles are well mixed as a solid solution without significant phase separation. Second, to confirm the component and composition of each element in the fabricated nanoparticles, X-ray photoelectron spectroscopy (XPS) and TEM–EDS were conducted (Figure 4c). XPS and EDS spectra shown in Figure 4c and Figure S5, Supporting Information, respectively, revealed that considerable amounts of Pt, Ru, and Ni are detected. In addition, after CTS, the elements were mainly found to be in the metallic state compared to the oxidation state before CTS (Figure S7, Supporting Information). However, owing to atmospheric oxidation, some of the oxidation states were also detected in the synthesized nanoparticles. In addition, the chloride peak was confirmed to almost disappear after the fabrication of multi-metallic nanoparticles (Figures S8–S10, Supporting Information), indicative of the change in the precursor state (metal chloride) to the metal state by CTS. Furthermore, the atomic composition of the components was analyzed by XPS and TEM–EDS, and the elemental composition of the $Pt_{0.65}Ru_{0.30}Ni_{0.05}$ alloy was determined: 73.9–77.8% for Pt, 18.6–21.5% for Ru, and 3.6–4.6% for Ni. The composition of the synthesized nanoparticles was different from the precursor composition loaded for the synthesis of ternary nanoparticles, which was related to different properties of each metal, for example, vapor pressure and phase transition temperature.[40] However, such a deviation between the composition of the precursor mixture and that of the fabricated nanoparticles is not concerning in the active-learning process as the machine considers every factor, including the composition of the synthesized nanoparticles that can affect the catalyst performance when its output is expected. In fact, this is a better method of

predicting the performance as it is barely possible to exactly match the composition of the precursor mixture with that of the actual fabricated elements by experiments.

2.6. Electrochemical Analysis of Synthesized Catalysts

By analyzing the performance of the catalyst, we were able to find a combination of catalysts showing the same tendency for overpotential along with other performances. In this study, it is very important that the experimental results and the results predicted through active learning show the same trend as the iteration proceeded. It is a great advantage that the results of active learning and experiments have the same tendency in the process of iteration without considering other characteristics such as the actual composition of the alloy, surface area and loading amount of the catalyst, and impedance of the catalyst as the input data.

Among the hydrogen evolution catalysts tested in this study, the $Pt_{0.65}Ru_{0.30}Ni_{0.05}$ catalyst found by active learning exhibited the best performance by each electrochemical method, which was in agreement with the active-learning result. First, the overpotential of the $Pt_{0.65}Ru_{0.30}Ni_{0.05}$ catalyst was significantly lower than those of the pure Pt catalyst and the $Pt_{0.7}Ru_{0.3}$ catalyst synthesized by the same method (i.e., 68.2 and 65.6 mV), respectively (Figure 4d). Although the $Pt_{0.65}Ru_{0.30}Ni_{0.05}$ catalyst exhibited the best performance, other binary catalysts (i.e., $Pt_{0.7}Ru_{0.3}$ or $Pt_{0.31}Ni_{0.69}$ catalyst) also exhibited performance better than that of each of the unary catalysts. Tafel and Nyquist plots were also fitted for unary catalysts and the best performing catalyst to understand the electrochemical behavior and verify its tendency with the active-learning result (Figure 4e and Figure S13, Supporting Information). By measuring the Tafel slope, the rate-determining step of HER can be determined as reported previously.[44,45] The Tafel slope of the $Pt_{0.65}Ru_{0.30}Ni_{0.05}$ catalyst was lower than that of Pt, which indicated hydrogen desorption over the $Pt_{0.65}Ru_{0.30}Ni_{0.05}$ catalyst occurred more efficiently than that over the Pt catalyst. In addition, Nyquist plots were compared to estimate the charge-transfer resistance (R_{ct}) of the catalyst. Notably, the comparison of the semicircle diameter revealed that the R_{ct} of the $Pt_{0.65}Ru_{0.30}Ni_{0.05}$ catalyst is considerably less than those of unary metal systems, suggesting rapid electron transfer.

To investigate the stability of the catalyst and its compositions, leaching of the metals before and after the reaction was observed as well as the stability when constant current was applied. After 1000 cycles from 0 to –0.15 V, about 2.25 μg of metals were leached in the electrolyte (Table S3, Supporting Information). Also, almost no degradation was observed after applying constant current density (10 mA cm^{-2}) for more than 300 minutes (Figure S14, Supporting Information).

The electrochemical analyses not only confirmed the outstanding electrochemical performance of the $Pt_{0.65}Ru_{0.30}Ni_{0.05}$ catalyst compared with those of the other catalysts fabricated herein, but also simultaneously validated the correspondence of experimental and the active-learning result. Therefore, the results of this study show that our proposed method can simplify the problem when trying to find a catalyst with the desired performance.

3. Conclusion

A system was constructed in which a machine can iteratively cooperate with the user to narrow down to the desired region with a relatively small amount of information while simultaneously utilizing only the information of the precursor mixture composition as input, and the other factors that affect the performance were considered. Initial data were provided to the system to construct the model, and it obtained a remarkable outperforming system after a number of iterations due to active learning. Overall, by active learning, the optimal component and composition of the well-performing catalyst for HER were found by a cost-efficient route with time savings. Thus, by effectively building the model and providing the required data to the model, a catalyst with an optimal component and composition can be efficiently determined regardless of its own experimental system without considering the catalytic background of each system. Thus, these results can be applied to other catalytic reaction fields, which can significantly simplify the problem of searching for efficient components and compositions of catalysts.

4. Experimental Section

Preparation of a Carbon Nanofiber Substrate: First, 2 g of polyacrylonitrile (PAN, 150 000 Mw, Sigma-Aldrich) was dissolved in 13 g of *N*,*N*-dimethylformamide (99.8%, Sigma-Aldrich) with magnetic stirring (at room temperature, 300 rpm), affording a polymeric ink solution. After the solution was homogeneously stirred at 80 °C for 12 h, electrospinning was conducted. The polymer solution was placed in a syringe with a metal nozzle (23 G), and a voltage of 10 kV was applied between the collector and the metal nozzle. The distance from the needle to the collector was fixed at 20 cm, and the feeding rate was 10 μL min^{-1}. After electrospinning, the free-standing PAN NF membrane that was attached to the collector was gently detached with tweezers. The PAN nanofibers were stabilized in air at 553 K for 1 h and carbonized under argon at 1173 K for 2 h.

Preparation of the Precursor Solution: All precursors were purchased from Sigma-Aldrich, including chloroplatinic(IV) acid hydrate, cobalt(II) chloride, copper(II) chloride, nickel(II) chloride, tin(II) chloride, palladium(II) chloride, ruthenium(III) chloride hydrate, and iron(III) chloride hexahydrate. All precursor solutions were synthesized by mixing MCl_xH_y precursors (0.1 M) with the precursors dissolved in ethanol.

Fabrication of the Electrode: First, prepared substrates were attached to quartz using a silver paste and copper tape. After the substrates were fixed, and the solution was prepared, they were dropped on the substrate with heating at 80 °C. The total solution volume was 200 μL. After the evaporation of ethanol, the carbothermal shock was conducted to fabricate multi-metallic nanoparticles with heating at 300 ms under Ar.

Electrochemical Testing for the HER: Electrochemical testing of the electrodes was conducted using a biologic VSP potentiostat. In the cell, three electrodes were used: a counter electrode (carbon rod), a reference electrode (Ag/AgCl in 3 M NaCl), and a working electrode. The working electrodes were sampled with a platinum wire by using a silver paste. A 0.5 M H_2SO_4 solution (45 mL) was used as the electrolyte for the reaction while stirring. The potential calculated was IR-corrected by using a potentiostat, and cyclic voltammetry was conducted at a scan rate of 5 mV s^{-1} from 0.05 to –0.8 V versus RHE. Electrochemical impedance spectroscopy was conducted using the same conditions as mentioned above with –0.2 V versus RHE and a scan rate from 10 mHz to 100 kHz. Double-layer capacitance (C_{dl}) of the electrodes was calculated by the CV curves obtained from 0.368 V versus RHE to 0.468 V versus RIE with a scan rate from 10 to 500 mV s^{-1}.

Characterization: Scanning electron microscopy (Hitachi, S-4800) was employed to observe HEA nanoparticles on carbon nanofiber at an

accelerating voltage of 10 kV. TEM (Talos F200X) was employed at 200 kV for confirming nanoparticle fabrication. By using the high-angle annular dark-field scanning TEM (HAADF-STEM) mode, the sample morphology was analyzed. By energy-dispersive X-ray spectrometry, the ratio and distribution of the elements were confirmed. The chemical states of the samples were analyzed by XPS (Thermo VG Scientific, K-alpha), which was performed using a monochromatic Al Kα (1486.6 eV) X-ray source.

Active-Learning Iteration Procedure: The model was first trained with initial data comprising eight unary and 65 binary precursor compositions while simultaneously searching for a multi-metallic alloy catalyst comprising up to three components. The model was sufficiently trained to accurately predict in the binary space after two iteration loops by requesting 20 points with high uncertainty in each iteration loop. Then, the trained model was further extended to make predictions in ternary combinations of precursors, where ten ternary compositions with the highest estimated uncertainty for exploration and ten compositions with the lowest predicted overpotential for exploitation were requested in each iteration loop. After three iteration loops in the ternary data space, the active-learning iterations were terminated.

Supporting Information

Supporting Information is available from the Wiley Online Library or from the author.

Acknowledgements

M.K., M.Y.H., W.-B.J., and J.Y. contributed equally to this work. This research was funded by the Saudi Aramco-KAIST CO_2 Management Center. This research was supported by KAIST Institute for the NanoCentury. This research was also supported by the National Research Foundation (NRF) of the Korean Government through the Ministry of Science, ICT, and Future Planning (MSIP) ((NRF2021M3H4A6A01041234, NRF2018M3D1A1058633, NRF2019R1A2C1085081, NRF2019M3D1A2104101, and NRF2021M3H4A6A01045764).

Conflict of Interest

The authors declare no conflict of interest.

Data Availability Statement

The data that support the findings of this study are available from the corresponding author upon reasonable request.

Keywords

active learning, carbothermal shock, catalyst composition, hydrogen evolution reaction, multi-metallic catalysts

Received: November 3, 2021
Revised: February 17, 2022
Published online: March 18, 2022

[1] Y. Yao, Z. Liu, P. Xie, Z. Huang, T. Li, D. Morris, Z. Finfrock, J. Zhou, M. Jiao, J. Gao, Y. Mao, J. Miao, P. Zhang, R. Shahbazian-Yassar, C. Wang, G. Wang, L. Hu, *Sci. Adv.* **2020**, *6*, eaaz0510.
[2] B. X. Cao, C. Wang, T. Yang, C. T. Liu, *Scr. Mater.* **2020**, *187*, 250.
[3] J. L. Snider, V. Streibel, M. A. Hubert, T. S. Choksi, E. Valle, D. C. Upham, J. Schumann, M. S. Duyar, A. Gallo, F. Abild-Pedersen, T. F. Jaramillo, *ACS Catal.* **2019**, *9*, 3399.
[4] K. Ye, A. Cao, J. Shao, G. Wang, R. Si, N. Ta, J. Xiao, G. Wang, *Sci. Bull.* **2020**, *65*, 711.
[5] A. K. Singh, Q. Xu, *ChemCatChem* **2013**, *5*, 652.
[6] L. Chen, X. Chen, H. Liu, Y. Li, *Small* **2015**, *11*, 2642.
[7] F. Chen, K. Shen, J. Chen, X. Yang, J. Cui, Y. Li, *ACS Cent. Sci.* **2019**, *5*, 176.
[8] L. Huang, P. C. Chen, M. Liu, X. Fu, P. Gordiichuk, Y. Yu, C. Wolverton, Y. Kang, C. A. Mirkin, *Proc. Natl. Acad. Sci. USA* **2018**, *115*, 3764.
[9] D. Wang, H. L. Xin, R. Hovden, H. Wang, Y. Yu, D. A. Muller, F. J. DiSalvo, H. D. Abruna, *Nat. Mater.* **2013**, *12*, 81.
[10] J. Kim, Y. Lee, S. Sun, *J. Am. Chem. Soc.* **2010**, *132*, 4996.
[11] K. Li, Y. Li, Y. Wang, J. Ge, C. Liu, W. Xing, *Energy Environ. Sci.* **2018**, *11*, 1232.
[12] N. Cheng, S. Stambula, D. Wang, M. N. Banis, J. Liu, A. Riese, B. Xiao, R. Li, T. K. Sham, L. M. Liu, G. A. Botton, X. Sun, *Nat. Commun.* **2016**, *7*, 13638.
[13] L. Bu, J. Ding, S. Guo, X. Zhang, D. Su, X. Zhu, J. Yao, J. Guo, G. Lu, X. Huang, *Adv. Mater.* **2015**, *27*, 7204.
[14] J. Mahmood, F. Li, S. M. Jung, M. S. Okyay, I. Ahmad, S. J. Kim, N. Park, H. Y. Jeong, J. B. Baek, *Nat. Nanotechnol.* **2017**, *12*, 441.
[15] D. H. Kweon, M. S. Okyay, S. J. Kim, J. P. Jeon, H. J. Noh, N. Park, J. Mahmood, J. B. Baek, *Nat. Commun.* **2020**, *11*, 1278.
[16] S. Štrbac, I. Srejić, Z. Rakočević, *J. Electrochem. Soc.* **2018**, *165*, J3335.
[17] Q. Zhang, Z. Duan, Y. Wang, L. Li, B. Nan, J. Guan, *J. Mater. Chem. A* **2020**, *8*, 19665.
[18] W. Xu, S. Zhu, Y. Liang, Z. Cui, X. Yang, A. Inoue, H. Wang, *J. Mater. Chem. A* **2017**, *5*, 18793.
[19] G. Wang, J. Liu, Y. Sui, M. Wang, L. Qiao, F. Du, B. Zou, *J. Mater. Chem. A* **2019**, *7*, 14876.
[20] M. Schalenbach, F. D. Speck, M. Ledendecke, O. Kasian, D. Goehl, A. M. Mingers, B. Breitbach, H. Springer, S. Cherevko, K. J. J. Mayrhofer, *Electrochim. Acta* **2018**, *259*, 1154.
[21] B. H. R. Suryanto, Y. Wang, R. K. Hocking, W. Adamson, C. Zhao, *Nat. Commun.* **2019**, *10*, 5599.
[22] J. Su, Y. Yang, G. Xia, J. Chen, P. Jiang, Q. Chen, *Nat. Commun.* **2017**, *8*, 14969.
[23] H. Zhang, Z. Ma, G. Liu, L. Shi, J. Tang, H. Pang, K. Wu, T. Takei, J. Zhang, Y. Yamauchi, J. Ye, *NPG Asia Mater.* **2016**, *8*, e293.
[24] J. R. Kitchin, *Nat. Catal.* **2018**, *1*, 230.
[25] B. R. Goldsmith, J. Esterhuizen, J. X. Liu, C. J. Bartel, C. Sutton, *AIChE J.* **2018**, *64*, 2311.
[26] S. Back, K. Tran, Z. W. Ulissi, *ACS Catal.* **2019**, *9*, 7651.
[27] A. J. Chowdhury, W. Yang, E. Walker, O. Mamun, A. Heyden, G. A. Terejanu, *J. Phys. Chem. C* **2018**, *122*, 28142.
[28] A. Jain, S. P. Ong, G. Hautier, W. Chen, W. D. Richards, S. Dacek, S. Cholia, D. Gunter, D. Skinner, G. Ceder, K. A. Persson, *APL Mater.* **2013**, *1*, 011002.
[29] S. Kirklin, J. E. Saal, B. Meredig, A. Thompson, J. W. Doak, M. Aykol, S. Rühl, C. Wolverton, *npj Comput. Mater.* **2015**, *1*, 15010.
[30] R. Jinnouchi, R. Asahi, *J. Phys. Chem. Lett.* **2017**, *8*, 4279.
[31] Z. Li, S. Wang, W. S. Chin, L. E. Achenie, H. Xin, *J. Mater. Chem. A* **2017**, *5*, 24131.
[32] Z. W. Ulissi, M. T. Tang, J. Xiao, X. Liu, D. A. Torelli, M. Karamad, K. Cummins, C. Hahn, N. S. Lewis, T. F. Jaramillo, K. Chan, J. K. Nørskov, *ACS Catal.* **2017**, *7*, 6600.
[33] T. A. A Batchelor, J. K. Pedersen, S. H. Winther, I. E. Castelli, K. W. Jacobsen, J. Rossmeisl, *Joule* **2019**, *3*, 834.
[34] M. W. Glasscott, A. D. Pendergast, S. Goines, A. R. Bishop, A. T. Hoang, C. Renault, J. E. Dick, *Nat. Commun.* **2019**, *10*, 2650.

[35] Z. Huang, Y. Yao, Z. Pang, Y. Yuan, T. Li, K. He, X. Hu, J. Cheng, W. Yao, Y. Liu, A. Nie, S. Sharifi-Asl, M. Cheng, B. Song, K. Amine, J. Lu, T. Li, L. Hu, R. Shahbazian-Yassar, *Nat. Commun.* **2020**, *11*, 6373.
[36] W. B. Jung, H. Park, J. S. Jang, D. Y. Kim, D. W. Kim, E. Lim, J. Y. Kim, S. Choi, J. Suk, Y. Kang, I. D. Kim, J. Kim, M. Wu, H. T. Jung, *ACS Nano* **2021**, *15*, 4235.
[37] B. Settles, *Active Learning: Synthesis Lectures on Artificial Intelligence and Machine Learning*, Morgan & Claypool Publishers, San Rafael, CA, USA **2012**.
[38] N. Bernstein, G. Csányi, V. L. Deringer, *npj Comput. Mater.* **2019**, *5*, 99.
[39] J. S. Smith, B. Nebgen, N. Lubbers, O. Isayev, A. E. Roitberg, *J. Chem. Phys.* **2018**, *148*, 241733.
[40] Y. Yao, Z. Huang, P. Xie, S. D. Lacey, R. J. Jacob, H. Xie, F. Chen, A. Nie, T. Pu, M. Rehwoldt, D. Yu, M. R. Zachariah, C. Wang, R. Shahbazian-Yassar, J. Li, L. Hu, *Science* **2018**, *359*, 1489.
[41] C. Yang, B. H. Ko, S. Hwang, Z. Liu, Y. Yao, W. Luc, M. Cui, A. S. Malkani, T. Li, X. Wang, J. Dai, B. Xu, G. Wang, D. Su, F. Jiao, L. Hu, *Sci. Adv.* **2020**, *6*, eaaz6844.
[42] Z. P. Lu, H. Wang, M. W. Chen, I. Baker, J. W. Yeh, C. T. Liu, T. G. Nieh, *Intermetallics* **2015**, *66*, 67.
[43] B. X. Cao, C. Wanga, T. Yang, C. T. Liu, *Scr. Mater.* **2020**, *187*, 255.
[44] B. E. Conway, B. V. Tilak, *Electrochim. Acta* **2002**, *47*, 3571.
[45] T. Shinagawa, A. T. Garcia-Esparza, K. Takanabe, *Sci. Rep.* **2015**, *5*, 13801.